Sensitivity of internal wave energy distribution over seabed corrugations to adjacent seabed features

Farid Karimpour[1]**, Ahmad Zareei**[1]**, Joël Tchoufag**[1]
and Mohammad-Reza Alam[1],†

[1]Department of Mechanical Engineering, University of California, Berkeley, CA 94720, USA

Here we show that the distribution of energy of internal gravity waves over a patch of seabed corrugations strongly depends on the distance of the patch to adjacent seafloor features located downstream of the patch. Specifically, we consider the steady state energy distribution due to an incident internal wave arriving at a patch of seabed ripples neighbouring (i) another patch of ripples (i.e. a second patch) and (ii) a vertical wall. Seabed undulations with dominant wavenumber twice as large as overpassing internal waves reflect back part of the energy of the incident internal waves (Bragg reflection) and allow the rest of the energy to transmit downstream. In the presence of a neighbouring topography on the downstream side, the transmitted energy from the patch may reflect back; partially if the downstream topography is another set of seabed ripples or fully if it is a vertical wall. The reflected wave from the downstream topography is again reflected back by the patch of ripples through the same mechanism. This consecutive reflection goes on indefinitely, leading to a complex interaction pattern including constructive and destructive interference of multiply reflected waves as well as an interplay between higher mode internal waves resonated over the topography. We show here that when steady state is reached both the qualitative and quantitative behaviour of the energy distribution over the patch is a strong function of the distance between the patch and the downstream topography: it can increase or decrease exponentially fast along the patch or stay (nearly) unchanged. As a result, for instance, the local energy density in the water column can become an order of magnitude larger in certain areas merely based on where the downstream topography is. This may result in the formation of steep waves in specific areas of the ocean, leading to breaking and enhanced mixing. At a particular distance, the wall or the second patch may also result in a complete disappearance of the trace of the seabed undulations on the upstream and the downstream wave field.

Key words: geophysical and geological flows, internal waves, topographic effects

1. Introduction

   Internal waves play an essential role in the transport and also mixing in the stably stratified ocean through their contribution to the turbulence caused by local instabilities

† Email address for correspondence: reza.alam@berkeley.edu

and breaking of small-scale internal waves (Bühler & Holmes-Cerfon 2011). However, the mechanism(s) leading to the loss of energy of the waves and determination of the locations in the ocean where the energy of the low-mode internal waves is lost to turbulence are still unanswered questions (Ansong *et al.* 2015) and hence have been the subject of many studies. It is conjectured that the low-mode energy can be dissipated locally and the remaining energy is transferred and decayed through the interaction of low-mode tides with the undular bottom topography which leads to the conversion of internal waves to higher-mode waves with shorter wavelengths (Bühler & Holmes-Cerfon 2011; Li & Mei 2014). These shorter wavelength and higher-mode waves are more susceptible to breaking and hence to losing their energy to turbulence.

The generation and scattering of internal waves from bumpy bottoms in two-dimensional fluids was first studied by Baines (1971*a*,*b*) over a finite length topography. He found that from the interaction of an incident wave with wavenumber (k) with a bottom topography with wavenumber (k_b), three waves could be scattered with wavenumbers k, $k + k_b$ and $k - k_b$ (see also Bell 1975*a*,*b*; Mied & Dugan 1976). More recently, Müller & Liu (2000*a*,*b*) used the theory of characteristics to investigate the scattering in a finite depth two-dimensional fluid and studied the energy transmission as a function of the incident wave and bottom slope. Their observation suggests that the bottom topography shape is an important factor in the flux of the wave energy into higher-mode waves that can break more easily and cause mixing, where for example convex profiles were more efficient than concave profiles. However, these works focused on the understanding of internal waves on a limited, short bottom topography and it was only recently that Bühler & Holmes-Cerfon (2011) investigated the interaction of internal waves with a long undulating bottom (in a linearly stratified two-dimensional fluid using linear theory). They investigated the interaction of a low-mode internal wave over both regular and irregular long patches of ripples and observed the decay of internal tides over a finite-amplitude topography (with subcritical slope). They also reported that energy focusing occurs on a long single patch of ripples when resonance conditions were satisfied. Li & Mei (2014) employed the method of multiple-scale perturbation analysis and studied internal waves over small-amplitude, long topographies. They compared their findings with the results of Bühler & Holmes-Cerfon (2011) and observed good agreement, which showed that the wave decay is exponential in space. It is worth mentioning that Mei (1985) used for the first time the method of multiple-scale perturbation analysis to study the evolution and resonance of surface waves interacting with a finite-amplitude topography. He showed that multiple-scale perturbation analysis, which is based on fast- and slow-varying variables, guarantees a well-defined bounded solution for waves over a large range of topographies which has been a serious issue with the classical perturbation analysis method. There have also been efforts to seek solutions using the Green's function method for studying the interaction of waves with a bottom topography. For example, Balmforth & Peacock (2009) studied the conversion of barotropic tides into internal waves by the bottom topography with periodic obstacles using Green's function in an infinite depth ocean. Considering steep obstacles, it was found that the barotropic energy conversion rate depends on both topographical as well as wave characteristics including the slope of the topography, wave slope and the separation of the obstacles from each other. The Green's function method is also used for studying the scattering phenomenon by the bottom topography. For example, Mathur, Carter & Peacock (2014) used the Green's function to study internal tide scattering in a two-dimensional ocean. They studied the efficiency of isolated, large obstacles for scattering of tides and compared this

to the impact of small-scale topography for scattering. The key finding was that a large, critical ridge is the main source for scattering of a mode 1 internal tide while a small-amplitude topography has a scattering efficiency of approximately 5 %–10 % for a length of 1000–3000 km, which is substantially lower than a single ridge scattering efficiency.

It is known that if an internal wave travels over a patch of corrugated seabed where the wavenumber of the seabed is twice as large as the wavenumber of the incident internal wave, then the energy of the incident internal wave is partially reflected, partially transferred to other modes (higher and lower) and the rest keeps travelling, i.e. is transmitted downstream (e.g. Bühler & Holmes-Cerfon 2011). Reflection of waves as they travel in a periodic medium of double the wavenumber is commonly known as Bragg reflection (or resonance). The phenomenon was first discovered in the context of electromagnetic waves in the early 20th century (Bragg & Bragg 1913), and since then has been observed, elucidated and reported extensively in many other physical systems such as in solid state physics, optics and acoustics (e.g. Fermi & Marshall 1947; Kryuchkyan & Hatsagortsyan 2011), as well as in water waves (e.g. Mei 1985; Alam, Liu & Yue 2009*a*, 2010; Couston, Jalali & Alam 2017).

Of interest to this manuscript is the dynamics of internal waves over a patch of seabed corrugations in the presence of a reflecting object downstream of the patch. This interest is motivated by several observations of enhanced (by orders of magnitude) and intense mixing over rough topographies of the oceans and the claimed attribution of these observations to internal wave breaking (e.g. Ledwell *et al.* 2000; Garabato *et al.* 2004), as well as reports of strong internal wave generation over an undular seabed (e.g. Kranenburg, Pietrzak & Abraham 1991; Pietrzak *et al.* 1991; Labeur & Pietrzak 2004; Pietrzak & Labeur 2004; Stastna 2011).

We present here analytically, through multiple-scale perturbation analysis supported by direct simulation, that the spatial evolution of internal wave energy and the interplay between modes over a patch of seabed undulations can be strongly dependent upon the distance of the patch from the neighbouring seabed features. We show that accumulation of internal wave energy may be an order of magnitude larger at specific areas of a patch, solely based on where the neighbouring features are. The physics behind this phenomenon lies in the constructive and destructive interference of multiply reflected waves: if a patch of seabed undulations satisfies the Bragg condition with internal waves, as mentioned above, it reflects part of the incident wave energy but allows the rest to transmit. The transmitted wave then gets reflected back by the downstream reflector. But this reflected wave again reflects back from the patch of undulations via the Bragg mechanism. This sequence of reflections continues indefinitely as multiply reflected waves add up and via constructive and/or destructive interference result in a very much different spatial distribution of energy over the patch than what is expected in the absence of the downstream topography. This phenomenon is a close cousin of the Fabry–Pérot interference in optics through which two partially reflecting mirrors trap light (Fabry & Pérot 1897). It has also been determined in the context of surface gravity waves in a homogeneous (unstratified) fluid where many features similar to the optics counterparts are found (Yu & Mei 2000; Couston *et al.* 2015). In the context of internal waves in a continuously stratified fluid, nevertheless, the problem is significantly different as here Bragg resonance leads to the generation of an infinite number of internal wave modes simultaneously exchanging energy with each other through the seabed, creating a complex pool of interacting waves. We would like to comment that for the case of internal waves there is another possibility for realizing the Fabry–Pérot interference

and that is through partial reflection of an internal wave beam from locations of critical stratification (see Mathur & Peacock 2010). For this to occur, a specific form of nonlinear density stratification is necessary.

Real seabed topography in the ocean is usually composed of many Fourier components and, likewise, internal waves often arrive in a group forming a spectrum of frequencies and wavenumbers. Therefore, several interaction conditions may be satisfied simultaneously resulting in a substantial energy exchange that may lead to significant change in the spectral density function of internal waves. The sensitivity mechanism elucidated here sheds light on the importance of the details of topographic features on the resulting spatial distribution of wave activity, and may help pinpoint areas of the ocean where appreciable mixing is expected.

In this manuscript, we start by presentation of the problem formulation (§ 2), followed by the multiple-scale perturbation analysis and the discussion of reflection and transmission amplitudes (§ 3). In § 4 (results and discussion), we first present the case of wave reflection by a single patch of ripples (§ 4.1), then study the case of a patch next to a reflective wall (§ 4.2) and then elaborate on the effect of a downstream patch of ripples on wave energy amplification (§ 4.3). We provide concluding remarks on our findings in § 5 and briefly comment on the relevance of the presented physics to the real ocean.

2. Governing equations

We consider an inviscid, incompressible, non-rotating, two-dimensional and stably stratified fluid with small-amplitude waves such that nonlinear advection terms can be neglected. We put the Cartesian coordinate system on the seabed, with z axis pointing upward (figure 1). The density of this stably stratified fluid is $\rho(x, z, t) = \overline{\rho}(z) + \rho'(x, z, t)$, where $\overline{\rho}$ is the background density (density at equilibrium) and ρ' is the density perturbation. Similarly, pressure is $p = \overline{p}(z) + p'(x, z, t)$ where $\overline{p}(z)$ satisfies the hydrostatic balance with the quiescent density as $\partial \overline{p}(z)/\partial z = -\overline{\rho}(z)g$, and p' is the pressure perturbation. The governing equations for the velocity $\boldsymbol{u} = (u, w)$, density and pressure perturbations ρ', p' are (e.g. Kundu, Cohen & Dowling 2012)

$$\frac{\partial u}{\partial t} + \frac{1}{\rho_0}\frac{\partial p'}{\partial x} = 0, \tag{2.1a}$$

$$\frac{\partial w}{\partial t} + \frac{1}{\rho_0}\frac{\partial p'}{\partial z} = -\frac{\rho' g}{\rho_0}, \tag{2.1b}$$

$$\frac{\partial u}{\partial x} + \frac{\partial w}{\partial z} = 0, \tag{2.1c}$$

$$\frac{\partial \rho'}{\partial t} - \frac{N^2 \rho_0}{g}w = 0, \tag{2.1d}$$

where $N = \sqrt{(-g/\rho_0)\partial\overline{\rho}/\partial z}$ is the buoyancy frequency and $\rho_0 = \overline{\rho}(z = H)$ is the density at the free surface. In (2.1), equations (2.1a) and (2.1b) are momentum equations, equation (2.1c) is the continuity equation and (2.1d) is obtained from linearizing the density equation which expresses the incompressibility of a fluid particle. Assuming a rigid-lid condition at the surface $z = H$ and that the deviation of the seabed from the mean depth is given by $h(x)$, boundary conditions for the governing equations (2.1) are

$$w = 0, \quad z = H; \quad w = u\frac{\partial h(x)}{\partial x}, \quad z = h(x), \tag{2.2a-d}$$

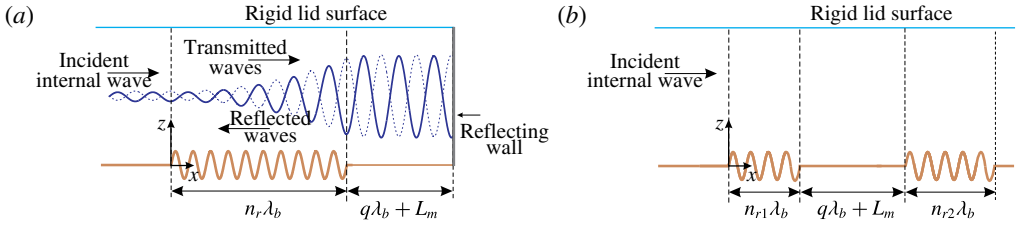FIGURE 1. (Colour online) Schematic representations of configurations considered here. (a) An incident internal wave of wavelength λ_i arrives from the far left to a patch of n_r seabed ripples of wavelength λ_b. There is a reflecting wall at a distance $q\lambda_b + L_m$, $(L_m < \lambda_b)$ measured from the end of the last ripple. (b) An incident internal wave of wavelength λ_i arrives from the far left to two patches of n_{r1} and n_{r2} seabed ripples of wavelength λ_b which are $q\lambda_b + L_m$ $(L_m < \lambda_b)$ apart. We will show that the energy distribution over the patch and in the area between the patch and the wall (a) or between the two patches (b) strongly depends on L_m.

where the bottom topography $h(x)$ has finite amplitude and subcritical slope, i.e. $|dh/dx| < 1$.

Since the flow field is two-dimensional and divergence free, the velocity can be written in terms of a streamfunction $\Psi(x, z, t)$ where $u = \partial\Psi/\partial z$ and $w = -\partial\Psi/\partial x$. Recasting governing equations (2.1) in terms of Ψ, we obtain

$$\frac{\partial^2}{\partial t^2}\left(\frac{\partial^2}{\partial x^2}\Psi + \frac{\partial^2}{\partial z^2}\Psi\right) + N^2\frac{\partial^2}{\partial x^2}\Psi = 0, \tag{2.3}$$

with the boundary conditions

$$\Psi(x, H, t) = \Psi(x, h(x), t) = 0. \tag{2.4}$$

We now consider time-harmonic solutions to (2.3) in the form $\Psi(x, z, t) = \text{Re}[\psi(x, z)e^{-i\omega t}]$ where ω is the frequency of the motion. Considering a constant N, we define scaled horizontal and vertical variables $x^* = \mu\pi x/H$, $z^* = \pi z/H$, and $h^* = \pi h/H$ where $\mu = \sqrt{\omega^2/(N^2 - \omega^2)}$. By this specific choice of scaling we will have an integer number of waves in the domain $0 \leqslant x^* \leqslant 2\pi$. This, later on, will help us to write the solution in terms of a Fourier series.

Using defined scaled variables, the governing equation (2.3) turns into (e.g. Bühler & Holmes-Cerfon 2011)

$$\frac{\partial^2}{\partial x^2}\psi - \frac{\partial^2}{\partial z^2}\psi = 0, \tag{2.5}$$

where here (and in what follows) asterisks are dropped for notational simplicity. Note that physical parameters (e.g. N, H) are hidden in the scaled variables. Similarly, the dimensionless form of the boundary condition (2.4) is obtained as

$$\psi(x, \pi, t) = \psi(x, h(x), t) = 0. \tag{2.6}$$

3. Perturbation analysis

We use multiple-scale perturbation analysis (cf. e.g. Li & Mei 2014) to solve for the wave field over a patch of small-amplitude ripples (i.e. $h(x)/H \ll 1$) in the area

$0 \leqslant x \leqslant L$. (Alternatively, the method of characteristics can be used and will lead to the same results (e.g. cf. Bühler & Holmes-Cerfon 2011).) We assume that at steady state the wave field variables are functions of spatial variables x, z and a slow horizontal scale $X = \epsilon x$ in which $\epsilon \ll 1$ is a measure of the waves steepness. We also assume that the solution to (2.5), i.e. $\psi(x, z, X)$, is periodic and that it can be expressed in terms of the following convergent series

$$\psi(x, z, X) = \psi^{(0)}(x, z, X) + \epsilon \psi^{(1)}(x, z, X) + O(\epsilon^2). \tag{3.1}$$

Substituting (3.1) in (2.5) and collecting terms of the same order, at orders $O(1)$ and $O(\epsilon)$ we obtain,

$$O(1): \quad \frac{\partial^2}{\partial x^2} \psi^{(0)} - \frac{\partial^2}{\partial z^2} \psi^{(0)} = 0, \tag{3.2a}$$

$$O(\epsilon): \quad \frac{\partial^2}{\partial x^2} \psi^{(1)} - \frac{\partial^2}{\partial z^2} \psi^{(1)} = -2\epsilon \frac{\partial^2}{\partial x \partial X} \psi^{(0)}. \tag{3.2b}$$

In a search for wave solutions to the original equation (2.5), we consider the following general solution to (3.2a)

$$\psi^{(0)}(x, z, X) = \sum_{m=1}^{\infty} [\widehat{T}_m(X) e^{imx} + \widehat{R}_m(X) e^{-imx}] \sin mz, \tag{3.3}$$

where $\widehat{T}_m, \widehat{R}_m$ are the streamfunction amplitudes of transmitted and reflected waves respectively. Therefore $\widehat{T}_m / \widehat{T}_\ell(0)$ is the transmission coefficient of mode m, where $\widehat{T}_\ell$ is the amplitude of incident internal wave of mode ℓ. If we assume the amplitude of the incident wave $\widehat{T}_\ell(0)$ is unity (which is a natural assumption), then $\widehat{T}_m, \widehat{R}_m$ are directly the transmission and reflection coefficients. Note that m is the mode number and an outcome of the scaling both in the horizontal and the vertical directions. The specific form of solution (3.3) assumes that these amplitudes can slowly vary over the patch of seabed corrugations. Upon substitution of (3.3) in (3.2b) we obtain

$$\frac{\partial^2 \psi^{(1)}}{\partial x^2} - \frac{\partial^2 \psi^{(1)}}{\partial z^2} = -2i \sum_{m=1}^{\infty} m \left[\frac{\partial \widehat{T}_m(X)}{\partial X} e^{imx} - \frac{\partial \widehat{R}_m(X)}{\partial X} e^{-imx} \right] \sin mz. \tag{3.4}$$

Coefficient $\partial \widehat{T}_n / \partial X$ ($\partial \widehat{R}_n / \partial X$) is readily obtained by multiplying both sides of (3.4) by $e^{-inx} \sin nz$ ($e^{inx} \sin nz$) and integrating over $z \in [0, \pi]$ and $x \in [0, L']$, where L' is the smallest integer multiplier of 2π which is greater than L. In other words, $L' = 2a\pi$ where a is an integer such that $(a - 1) < L/(2\pi) \leqslant a$. Coefficients $\partial \widehat{T}_n / \partial X$, ($\partial \widehat{R}_n / \partial X$) are obtained as:

$$\frac{\partial \widehat{T}_n}{\partial X} = \frac{-i}{\pi L'} \int_{x=0}^{L'} \psi^{(1)}(x, 0, X) e^{-inx} \, dx, \quad \frac{\partial \widehat{R}_n}{\partial X} = \frac{i}{\pi L'} \int_{x=0}^{L'} \psi^{(1)}(x, 0, X) e^{inx} \, dx, \tag{3.5a,b}$$

where integration by parts is used for the left-hand side of (3.4). Taylor expansion of the boundary condition (2.4) at $z = 0$, assuming $h(x)/H \sim O(\epsilon) \ll 1$, yields $\psi^{(1)}(x, 0, X) = -h(x) \psi_z^{(0)}(x, 0, X)$, and therefore

$$\frac{\partial}{\partial X} \left\{ \begin{matrix} \widehat{T}_n \\ \widehat{R}_n \end{matrix} \right\} = \frac{\pm i}{\pi L'} \int_{x=0}^{L'} h(x) \sum_{m=1}^{\infty} m[\widehat{T}_m(X) e^{imx} + \widehat{R}_m(X) e^{-imx}] e^{\mp inx} \, dx, \tag{3.6}$$

where the upper/lower signs are respectively for $\widehat{T}_n$ and $\widehat{R}_n$. For a general topography, we can further simplify (3.6), and write it as a system of ordinary differential equations as

$$\frac{\partial}{\partial X} \left\{ \begin{matrix} \widehat{T}_n \\ \widehat{R}_n \end{matrix} \right\} = \sum_{m=1}^{\infty} \left\{ \begin{matrix} \chi_{nm}^{11} \\ \chi_{nm}^{21} \end{matrix} \right\} \widehat{T}_m + \left\{ \begin{matrix} \chi_{nm}^{12} \\ \chi_{nm}^{22} \end{matrix} \right\} \widehat{R}_m, \tag{3.7}$$

where

$$\chi_{nm}^{ij} = \frac{\mathrm{i}(-1)^{i+1}}{\pi L'} \int_{x=0}^{L'} h(x) m \mathrm{e}^{\mathrm{i}x[(-1)^{j+1}m+(-1)^i n]} \, \mathrm{d}x. \tag{3.8}$$

If the bottom topography $h(x)$ in the region of $0 \leqslant x \leqslant L$ can be written in the form $h(x) = \sum_{k=-\infty}^{\infty} h_k \mathrm{e}^{\mathrm{i}kx}$, then (3.8) can further be simplified into

$$\chi_{nm}^{11} = \frac{\mathrm{i}m}{\pi} h_{n-m}, \quad \chi_{nm}^{12} = \frac{\mathrm{i}m}{\pi} h_{n+m}, \tag{3.9a,b}$$

$$\chi_{nm}^{21} = \frac{-\mathrm{i}m}{\pi} h_{-n-m}, \quad \chi_{nm}^{22} = \frac{-\mathrm{i}m}{\pi} h_{-n+m}. \tag{3.10a,b}$$

The vertical velocity transmission and reflection amplitudes (T_m, R_m) are obtained from $\widehat{T}_m, \widehat{R}_m$ through $T_m = -\mathrm{i}m\widehat{T}_m(X)$ and $R_m = \mathrm{i}m\widehat{R}_m(X)$. The spatially averaged kinetic and potential energy for each mode are obtained from $\langle E_n^k \rangle = (1/2)\rho_0(1/\lambda_n) \int_0^{\lambda_n} \mathrm{d}x \int_0^H \overline{(u_n^2 + w_n^2)} \, \mathrm{d}z$ and $\langle E_n^p \rangle = (1/\lambda_n) \int_0^{\lambda_n} \mathrm{d}x \int_0^H (g^2 \overline{\rho_n'^2})/(2\rho_0 N^2) \, \mathrm{d}z$, where the overbar denotes the temporal average and $\langle \cdot \rangle$ shows the spatial average over one wavelength (cf. figure 5 where this averaging has not been implemented). These equations result in

$$\langle E_n^k \rangle = \langle E_n^p \rangle = \frac{1}{8} \rho_0 A_n^2 \frac{N^2}{\omega^2} H = \frac{1}{8} \rho_0 (T_n^2 + R_n^2) \left(1 + \frac{k_{z,n}^2}{k_{x,n}^2} \right) H, \tag{3.11}$$

where k_z, k_x are vertical and horizontal wavenumbers respectively and $\lambda_n = 2\pi/k_{x,n}$. Hence, the total energy per unit area is

$$\langle E \rangle = \langle E^k \rangle + \langle E^p \rangle = \sum_{n=1}^{\infty} \frac{1}{4} \rho_0 (T_n^2 + R_n^2) \left(1 + \frac{k_{z,n}^2}{k_{x,n}^2} \right) H. \tag{3.12}$$

We define the normalized total energy by using the incident internal wave (mode ℓ) energy as the reference, i.e.

$$\widetilde{E} = \frac{\langle E \rangle}{\langle E_{incident} \rangle} = \sum_{n=1}^{\infty} \frac{T_n^2 + R_n^2}{T_{\ell,(x=0)}^2}. \tag{3.13}$$

It can also be shown that the normalized energy flux of transmitted (reflected) waves is a function of the velocity transmission (reflection) amplitudes, i.e.

$$F_n^T = \frac{\ell T_n^2}{n T_{\ell,(x=0)}^2}; \quad F_n^R = \frac{\ell R_n^2}{n T_{\ell,(x=0)}^2}, \tag{3.14a,b}$$

and hence the total energy flux is

$$F = \sum_{n=1}^{\infty} \ell \frac{T_n^2 - R_n^2}{n T_{\ell,(x=0)}^2}, \tag{3.15}$$

which for a steady state case has to be constant over the whole domain.

In (3.13) the total energy is normalized by the incident wave energy. We would like to emphasize that the group speeds of different modes are clearly different, and while the total energy flux over a finite patch (or patches) must remain constant in a steady state, the total energy in the water column per unit area ($\widetilde{E}$) may be very much different at different locations of the patch. Therefore, $\widetilde{E}$ is an important quantity as higher energy in the water column means taller (and hence steeper) waves which are more prone to breaking. This is similar to the shoaling of surface waves (e.g. Tsunamis): while the energy flux stays constant over a shoal, since the group speed decreases due to water depth decrease, the energy per unit area in the water column increases. This is manifested in the amplitude increase of the surface waves that results in nonlinear effects and eventually leads to wave breaking.

In solving (3.7) in practice, the infinite series must be truncated at a finite number of terms. The number of terms required is determined by the length of a patch, as longer patches allow higher internal wave modes to rise from zero, evolve and influence the overall dynamics. In numerical evaluation of the reflection and transmission amplitudes in the next section, we increase the number of modes until no further change over the patch is observed, i.e. we perform a numerical convergence test with respect to the number of modes. In the results of § 4, the chosen number of modes for a patch of approximately six wavelengths long is $O(200)$ modes.

4. Results and discussion

With the formulation of § 3 in hand, we now proceed to study the spatial evolution of the internal wave energy over a patch of seabed ripples. For the sake of completeness, we review the energy distribution over a single patch of ripples, and then focus our attention on: (i) a patch of seabed ripples located at distance $q\lambda_b + L_m$ from a vertical wall and (ii) two patches of ripples at the distance $q\lambda_b + L_m$ from each other (q being a non-negative integer number). We show that in both cases, the amplitudes of the different mode internal waves and the overall energy distribution strongly depend on L_m but are independent of q.

4.1. *Single patch*

In a continuously stratified fluid of constant N, and if normalization of § 2 is employed, then a frequency ω is associated with an infinite number of internal wave modes with integer wavenumbers. If an internal wave mode m propagates over a seabed undulation that has a component with the wavenumber $n_b = 2m$, then through Bragg resonance, new free-propagating internal waves of mode $m \pm n_b$ are excited (resonated). In general, for reflection to occur, the bottom wavenumber has to be equal to or greater than twice the first mode wavenumber, i.e. $n_b \geqslant 2m$. These two new waves can interact with the same topography to generate a new set of resonant waves $m + 2n_b$, and $m - 2n_b$. Eventually, and if the patch is long enough, an infinite number of waves with wavenumbers $m \pm jn_b$ and with integer $j \in (0, \infty)$ will appear in the water.

For illustration purposes, let us consider a mode 1 (i.e. $m = 1$) internal wave propagating over a monochromatic patch of ripples $h(x) = a_b \sin n_b x$, with $a_b = 4\pi/100$ (which implies the ripples amplitude is 4 % of the water depth) and $n_b = 2$. We consider a patch that extends over the area $0 \leqslant x \leqslant L = 6\lambda_b$ where $\lambda_b = 2\pi/n_b$ is the seabed ripples' wavelength. At $x = 0$, $T_1 = 1$ and $T_n = 0$ for $n > 1$. At $x = L$, $R_n = 0$. To
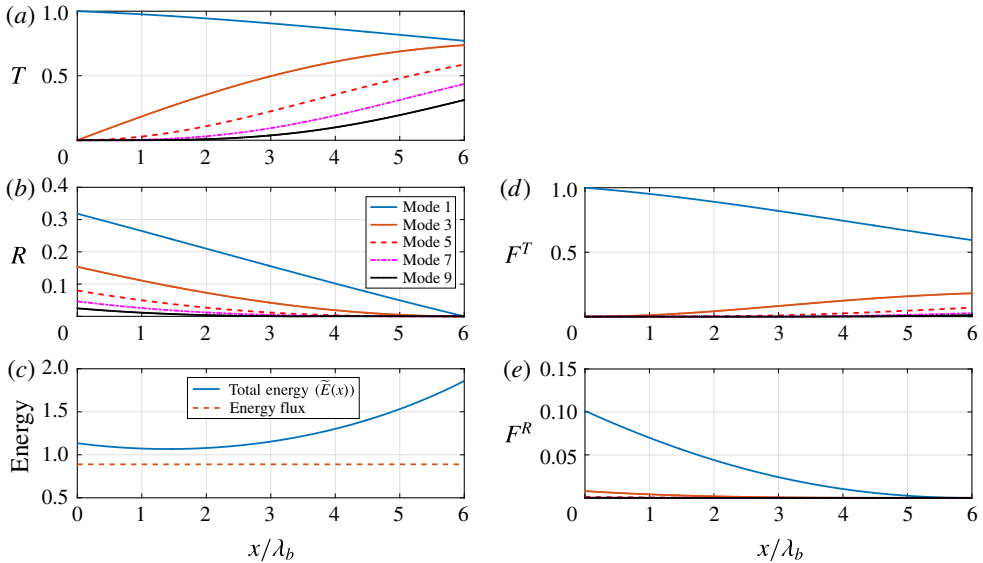
FIGURE 2. (Colour online) Interaction of a mode 1 incident internal wave ($m = 1$) with a single patch of sinusoidal ripples $h(x) = 0.04\pi \sin(2x)$ ($0 \leqslant x \leqslant 6\lambda_b$, i.e. the patch is composed of six ripples). Panels (*a*), (*b*) and (*c*) respectively show transmission amplitude T, reflection amplitude R and the normalized energy per unit area $\widetilde{E}$ over the patch. Panels (*d*) and (*e*) show energy flux of different modes in, respectively, the transmission and reflection directions. The energy of the incident wave (mode 1) decreases as energy goes to higher modes in transmission, as well as mode 1 and higher modes in reflection. The overall energy per unit area $\widetilde{E}$ initially decreases a little, but eventually takes off toward the downstream of the patch. Energy flux (dashed line in (*c*)) is constant over the patch, as expected.

reach a converged solution 200 modes are considered. The variation of the amplitude of the first four resonated waves along with the amplitude of the incident wave is shown in figure 2. Higher modes exist but are too small to be shown. An incident wave of mode $m = 1$ arrives from $-\infty$, and upon interaction with the seabed $n_b = 2$, generates new waves with wavenumbers $m + n_b = 3$ and $m - n_b = -1$ (the negative sign shows that this new wave, which is mode 1, moves in the opposite direction and hence appears in the reflection plot, see figure 2*b*). These newly generated waves pick up in amplitude at the cost of incident wave amplitude decaying over the patch, as is seen in figure 2(*a*). Once the amplitude of the mode 3 wave (red line) is large enough, through the same topography, mode 5 is resonated, and the interaction goes on. A similar story holds for the waves in reflection. The mode 1 wave in reflection resonates mode 3 and so on. While (3.7) gives us all modes that are generated here, we only present the first five resonant modes. Figure 2(*c*) shows the energy per unit area in the water column. Since the group velocity of higher modes is slower, energy is accumulated toward the end of the patch where more energy is in the higher modes that travel more slowly. As expected, in steady state the energy flux remains unchanged (energy flux is normalized by the energy flux of the incident wave). Note that energy density per unit area everywhere is greater than the incident wave energy density per unit area, and toward the end of the patch becomes much higher. This is clearly a result of the generation of internal waves with higher wavenumbers. We also

show in figure 2(d,e) the energy flux of each mode over the patch according to (3.14). Clearly, and as suggested by (3.14), energy flux decreases substantially for higher modes as their group speed is much lower. We would like to note that the focus in this study is on the case where the bottom wavenumber is twice as large as that of the internal waves, for which, as we will discuss, the behaviour is a strong function of the second (downstream) irregularity. The case of the wavenumber of the seabed undulations being the same as that of internal waves leads to only transmission and hence a downstream irregularity will not have any effect on the upstream patch (for a detailed study of different scenarios in this case, including the effect of detuning i.e. when the resonance condition is not perfectly satisfied, the reader is referred to Couston, Liang & Alam 2016).

4.2. *Patch–wall case*

Now let us assume that there is a wall on the downstream of the patch, at the distance $q\lambda_b + L_m$ (where $q \in \mathbb{N}^0$, i.e. it is a non-negative integer) from the end of the last ripple (cf. figure 1a). As waves propagate over the patch, a picture similar to figure 2 starts to form. Waves downstream, nevertheless, are reflected back by the wall and start to interact again with the topography. These left-propagating waves are partially transmitted, but also partially reflected back toward the wall. It turns out that the resulting effect is very complicated and a strong function of L_m.

We present in figure 3(a–c) the final steady state transmission/reflection amplitudes of different modes and energy per unit area over a patch of six ripples with a wall at the distance $L_m/\lambda_b = 0$, 0.25 and 0.50 respectively. The boundary condition at the wall is that the horizontal velocity must be zero. By plugging this condition into (3.3) for a perfectly reflective wall we obtain $T_n = R_n$. Other parameters of the ripples are the same as in §4.1. For $L_m/\lambda_b = 0$, energy goes from mode 1 to higher modes as the incident wave propagates over the patch. However, interestingly after reflection the energy entirely goes back to mode 1 such that in the upstream there is no reflected wave except mode 1. Energy per unit area $\widetilde{E}$ does not change much over the patch. The spatial evolution of modes for the case of $L_m/\lambda_b = 0.5$ is similar to the case of $L_m/\lambda_b = 0$, except that in the former the amplitude of mode 1 wave increases over the patch, resulting in a significant energy increase over the patch toward the downstream side. For the distance $L_m/\lambda_b = 0.25$, the transmission amplitudes figure is qualitatively similar to the case of $L_m/\lambda_b = 0$, but the reflection amplitudes figure is very much different: higher modes remain with non-zero amplitude (with finite energy) at the beginning of the patch and propagate upstream. This means that higher modes can be seen upstream of the patch moving toward the left (this is not the case for $L_m/\lambda_b = 0$, 0.5). In this case, $\widetilde{E}$ is highest at the beginning of the patch and decays fast toward the wall side of the patch. Note that the spatial distribution of energy is periodic with the wavelength λ_b and this can be shown to be also the case for each of wave modes involved. Therefore addition of $q\lambda_b$ (q being an integer number) to the distance between the patch and the wall does not affect the results shown here.

To see the behaviour of energy density per unit area for various L_m, figure 4 shows energy at the beginning of the patch (solid blue line) and at the end of the patch (dashed red line) as a function of L_m. Note that $\widetilde{E}$ is a continuous quantity which varies over the patch and its values at the beginning and end of the patch for different distances between the wall and the patch are shown to highlight the sensitivity of the internal waves energy distribution to the patch–wall distance. For $L_m/\lambda_b = 0$, 0.5 we, in fact, obtain minimum energy at the beginning of the patch. As shown in figure 3,
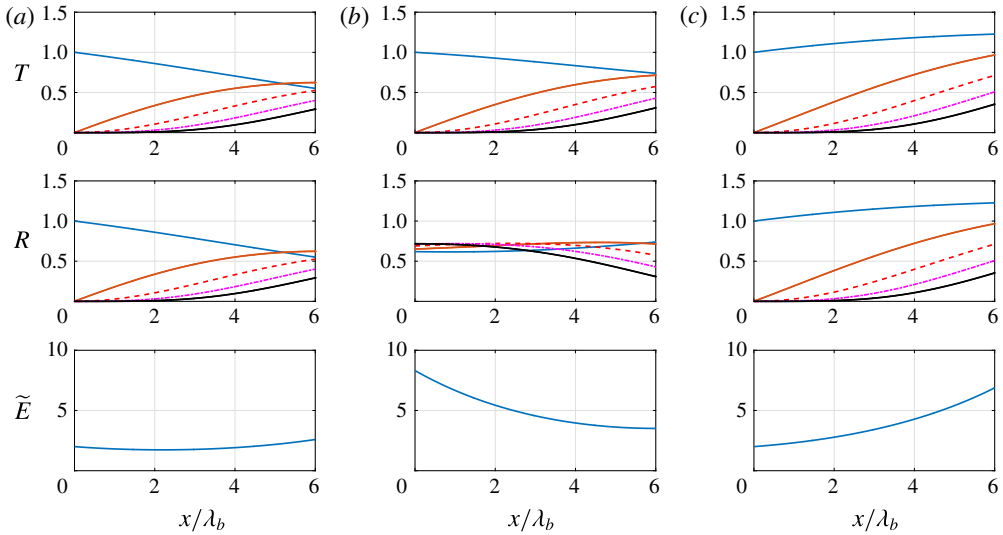
FIGURE 3. (Colour online) Variation of transmission amplitude (T), reflection amplitude (R) and the normalized energy per unit area $\widetilde{E}$ over the patch of $n_r = 6$ ripples, for a downstream wall at the distance (*a*) $L_m/\lambda_b = 0$, (*b*) $L_m/\lambda_b = 0.25$ and (*c*) $L_m/\lambda_b = 0.50$, from the end of the patch. Plotted are the mode 1 (——, blue), mode 3 (——, red), mode 5 (– – –, red), mode 7 (— · —, magenta) and mode 9 (——, black) internal waves. Higher modes exist, but are not shown here. Note that for $L_m/\lambda_b = 0$, 0.5 (*a,c*) through a complicated set of chain interactions all the energy eventually goes back to mode 1 on the upstream side of the patch. In this case an upstream observer does not see any trace of the patch of ripples. To this observer, everything looks like a perfect reflection from the wall in the absence of seabed irregularities. For any other value of L_m/λ_b, the upstream observer sees many other internal wave modes besides mode 1.

in both cases only a mode 1 wave appears upstream: incident and reflected waves together form a mode 1 standing wave upstream of the patch. Energy density near the wall, however, is maximum for $L_m/\lambda_b = 0.5$ and minimum for $L_m/\lambda_b = 0$. The other important extremum is $L_m/\lambda_b = 0.25$ for which $\widetilde{E}$ is maximum upstream as, in addition to mode 1, several higher-mode waves also reflect back toward the $-\infty$. The behaviour of the energy upstream is symmetric about $L_m/\lambda_b = 0.5$. Also seen in figure 4 is that for $n_r = 6$, $\widetilde{E}(0)$ may be affected by a factor of ~ 4 depending on L_m. For $n_r = 12$ (not shown here), it turns out this contrast is as big as 50 times.

To provide an independent cross-validation to the theoretical solution, we present here a comparison with results from direct simulation of (2.3). To this end, we used the open source solver FreeFem++ (Hecht 2012) based on the finite element method (FEM) to solve linear inviscid internal waves problems in two-dimensional configurations with a rigid lid at the top (see appendix A for details of the numerical implementation). These ripples have an amplitude of $a_b = 0.04\pi$ m and a wavelength $\lambda_b = \lambda_1/2 = 4.184$ m in order to satisfy the Bragg condition where λ_1 is the wavelength of the incident wave which is mode 1. We consider the case of a constant Brunt–Väisälä frequency of $N = 0.3534$ s^{-1}. At the left boundary where the wavemaker is located, a mode 1 internal wave is imposed through specifying the streamfunction as $\psi(z, t) = \psi_0 \sin(k_z z) \cos(\omega t)$ where $\omega \approx 0.212$ s^{-1}, $k_z = 1$ m^{-1} is the first mode vertical wavenumber and $\psi_0 = 0.013$ m^2 s^{-1}. Other boundary conditions
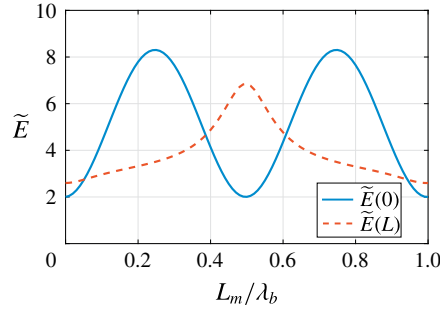
FIGURE 4. (Colour online) Spatial variation of energy per unit area $\widetilde{E}$ over the patch of bottom ripples ($n_r = 6$) for different distances of the patch from a reflecting wall downstream. The energy $\widetilde{E}$ is maximum at the beginning (upstream side) of the patch for $L_m/\lambda_b = 0.25$ and 0.75, and is maximum at the wall side (downstream side) of the patch for $L_m/\lambda_b = 0.5$.
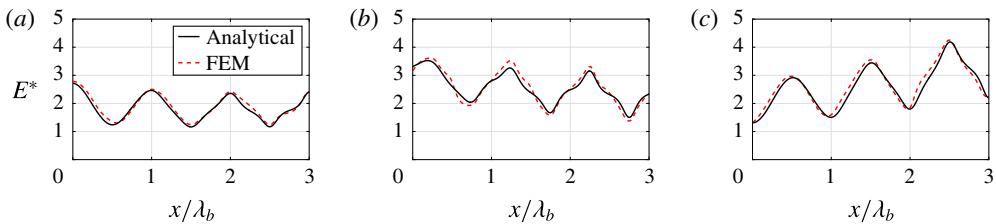

FIGURE 5. (Colour online) Comparison of energy per unit area (E^*) from analytical solution (——), FEM simulations (– – –), for respectively $L_m/\lambda_b = 0$, 0.25 and 0.5 in (a), (b) and (c).

are chosen as free slip at the bottom, a solid wall with no-normal velocity at the right end boundary and the rigid lid at the top surface. The height and length of the computational domain are respectively $H = \pi$ m and the domain length is $L_d = 15\lambda_1 + L_m \approx 125.513 + L_m$ m where $L_m \approx 0$, 2.092 and 4.184 m. The length of the domain is chosen such that steady state can be reached. The domain is discretized with triangular elements with a total number of $33\,290$ triangles. Also, a second-order implicit scheme is employed for the time discretization of the wave equation.

The comparison of spatial distribution of energy from theoretical predictions and those obtained by direct simulation from our FEM code is shown in figure 5 for $L_m/\lambda_b = 0$, 0.25 and 0.50. In this figure, E^* is the total energy normalized by the total energy of the incident wave (E_ℓ) and is calculated as $E^* = (E^k + E^p)/E_\ell$, where the kinetic energy (E^k) and the potential energy (E^p) are $E^k = \sum_{n=1}^{\infty} 1/2\rho_0 \int_0^H (\overline{u_n^2 + w_n^2})\,\mathrm{d}z$ and $E^p = \sum_{n=1}^{\infty} \int_0^H (g^2\overline{\rho_n'^2})/(2\rho_0 N^2)\,\mathrm{d}z$ (note that $\widetilde{E}$ is the spatial average of E^*). E^* is chosen here for validation because the horizontal spatial average ($\widetilde{E}$) of the energy over the patch is not possible from numerical simulation results and would cause errors. Three ripples (instead of six as before) are chosen for validation because this requires a smaller domain and a smaller simulation time to reach steady state. As can be seen, theoretical predictions and direct simulation results show good agreement with each other.
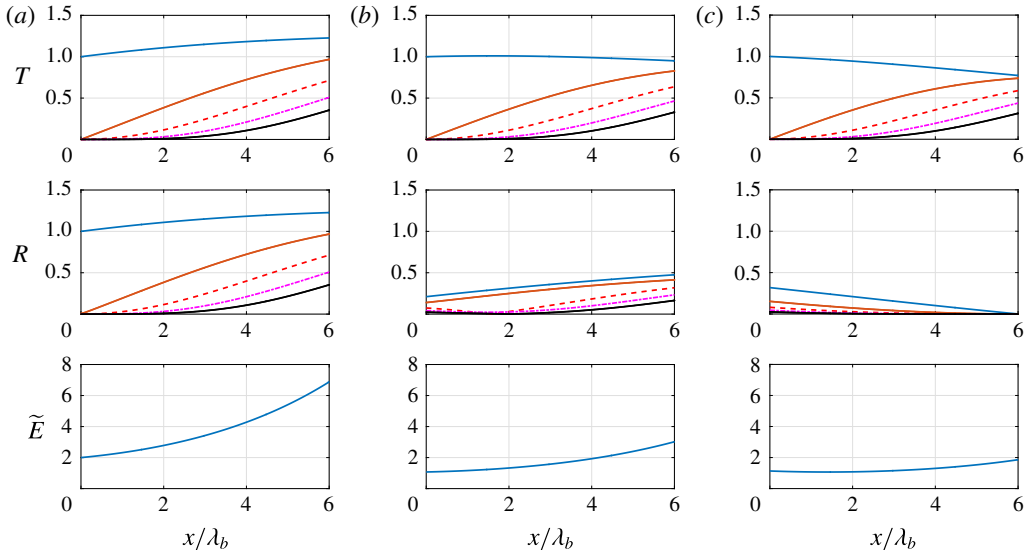
FIGURE 6. (Colour online) Effect of the wall reflectivity on the transmission (T) and reflection (R) amplitudes and on the normalized energy per unit area $\tilde{E}$. Panels (a)–(c) respectively correspond to wall reflectivity of 100 % (i.e. perfect reflector and the same as figure 3c), 50 % and 0 % (i.e. perfect absorber) and in all three cases $L_m/\lambda_b = 0.5$ which corresponds to the maximum $\tilde{E}$ at the end of the patch $L = n\lambda_b$. Plotted in figures for T, R are mode 1 internal wave (——, blue), mode 3 (——, red), mode 5 (– – –, red), mode 7 (— · —, magenta) and mode 9 (——, black).

Clearly the amplification of the energy occurs due to the reflection from the wall and hence the observed energy directly depends on the reflectivity of the wall. The considered wall in this study is a simplified model for a finite-height ridge or a continental slope in real oceans, which have a finite height and hence cannot fully reflect the incident waves. This warrants the need to assess the effect of the reflectivity index on the energy amplification. To better understand this effect, we consider 3 different cases for which the reflectivity index = 100 % (perfect reflection), 50 % and 0 % (perfect absorption). This is shown in figure 6(a–c), where the transmission/reflection amplitudes of different modes and energy per unit area $\tilde{E}$ are plotted for $L_m/\lambda_b = 0.5$ which has the maximum energy amplification at the end of the patch $\tilde{E}(L_m)$. The first case of perfect reflection is the same as figure 3(c). As discussed previously, the transmission and reflection amplitudes are identical and $\tilde{E}(L_m) \approx 7$. If the wall reflectivity index is 50 % (figure 6b) then $\tilde{E}(L_m) \approx 3$ and both T and R decrease while the decrease of the reflection amplitudes is more significant. Ultimately, zero reflectivity (i.e. the wall is a perfect absorber, figure 6c), means that the wall has no role and it is identical to a single patch case (see figure 2). Here, $\tilde{E}(L_m) \approx 1.8$ and the transmission amplitude, especially the first mode attenuates compared to the other two cases. Also, as expected, all reflection amplitudes are fully zero at the wall and slightly increase towards the beginning of the patch. In order to further assess the impact of the reflectivity index on the energy distribution, the energy at the beginning $\tilde{E}(0)$ and end $\tilde{E}(L)$ of a six ripple patch is plotted in figure 7 as a function of reflectivity index, where $L_M/\lambda_b = 0.5$. The results show that with the increase of the reflectivity index the energy amplifies especially at the
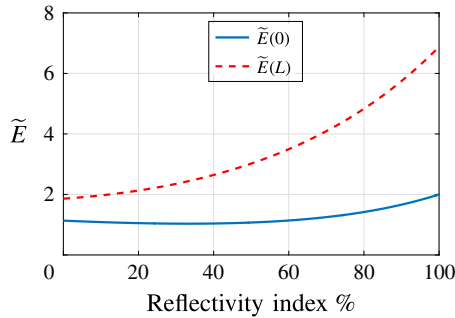
FIGURE 7. (Colour online) Variation of energy per unit area $\widetilde{E}$ at the beginning and end of a six ripple bottom patch ($n_r = 6$) as a function of the wall reflectivity index. The energy $\widetilde{E}$ is calculated for patch–wall distance of $L_m/\lambda_b = 0.5$.

end of the patch. Results from figures 6 and 7 generally suggest that the strength of amplification has an algebraic dependence on the wall reflectivity index.

We would like to briefly comment about the effect of viscosity here. Viscous dissipation within linear internal waves can be estimated by a linear approximation (Baines 1998, §4.7) and can be shown to be very small. For instance for a mode 1 internal wave under the parameters of the case presented in figure 5 and for a water depth of $H = 100$ m, it can be shown that the rate of decay of vertical displacement is less than one per cent over the distance of 1000 km. Clearly if waves are steep, then nonlinear effects dominate the viscous dissipation and results potentially orders-of-magnitude different from the linear approximation may be obtained. In an extreme nonlinear case of the wave breaking, almost the entire energy of a wave is dissipated over a distance comparable to the wave's wavelength (Gargett & Holloway 1984; Lamb 2014).

Turbulent (eddy) viscosity (ν_t) is much higher than molecular viscosity (ν) in the ocean, especially in the mixed layer. However, it should be noted that the turbulent viscosity only bridges between the turbulent fluxes (i.e. turbulent momentum fluxes) and the mean shear rate (S). For example, in a one-dimensional flow $\overline{u'w'} = -\nu_t S$, where $\overline{u'w'}$ is the turbulent momentum flux (Reynolds stress) and in our study $S = \partial \overline{U}/\partial z$ where $\overline{U}$ is the mean horizontal velocity and z is the vertical distance from the reference at the bottom. Regardless of the value of the turbulent viscosity (ν_t), the fluxes are a function of S, which is low in our study so this consequently minimizes the production of the turbulent kinetic energy and turbulence effects and hence the dissipation of energy in the flow.

To assess the effect of viscosity on the mechanism elucidated in this article, we investigated the results of simulations, both inviscid and in the presence of viscosity with kinematic viscosity $\nu = 10^{-6}$, 10^{-3} m^2 s^{-1}, performed with the open source code SUNTANS (the Stanford unstructured non-hydrostatic terrain-following adaptive Navier–Stokes simulator). SUNTANS is a finite volume solver developed for simulation of three-dimensional non-hydrostatic internal waves in the ocean (Fringer, Gerritsen & Street 2006) and since its introduction in 2006, it has undergone cross-checks extensively (e.g. Fringer & Zhang 2008; Wang *et al.* 2009; Kang & Fringer 2012). SUNTANS only uses a free surface boundary condition, and therefore does not completely agree with our theory (which is based on the rigid-lid assumption). However, it enables us to numerically study the effect of viscosity. The

domain dimensions for our simulations are $H = 100$ m and $L = 14\lambda_1 = 3728.5$ m and chosen such that there is enough time for the steady state to be reached. The grid resolution is 1000×100 in respectively the x and z directions. Given the different domain dimensions between the FEM set-up and SUNTANS, the essential variables (such as bottom height to depth ratio, μ, etc.) are chosen such that they match with the FEM set-up. Thus the three ripples have an amplitude of 4 m. The buoyancy frequency is chosen as $N = 0.0443$ s^{-1} for an incident mode 1 wave with frequency $\omega = 0.0266$ s^{-1} and vertical wavenumber $m_1 = 0.0315$ m^{-1} which result in the same μ as used in the FEM simulation. Also, the cross-shore velocity amplitude is $U_0 = 0.013$ m s^{-1}. All the boundary conditions imposed in SUNTANS are similar to FEM simulation except the free surface on the top. As mentioned earlier, the free surface is used as the boundary condition in the numerical simulations because SUNTANS does not offer rigid-lid boundary condition. Our simulations show a maximum difference of less than 7 % between inviscid and viscous simulations with $\nu = 10^{-6}$, 10^{-3} m^2 s^{-1}, confirming that the effect of viscosity is negligible for the current study.

4.3. *Two patch case*

Now let us consider a second patch of ripples downstream of the patch under investigation (figure 1*b*). For presentation purposes, we assume that the ripples in both patches have the same normalized wavenumber $n_b = 2$ and amplitude $a_b = 4\pi/100$. The distribution of energy on each patch, and in the area between the two patches, similar to the case of § 4.2 is strongly dependent on L_m (the distance between the two patches). Distribution of energy density $\widetilde{E}$ for $L_m/\lambda_b = 0$, 0.125, 0.250, 0.375 and 0.500 is shown in figure 8(*a*) for two identical patches of $n_r = 4$ seabed ripples. Note that the actual distance between the patch in each case is $q\lambda_b + L_m$ (q positive integer) where in the case of figure 8(*a*), $q = 4$. But as before q does not play any role and it is L_m that determines the energy distribution. Figure 8(*a*) shows that for $L_m/\lambda_b = 0$, 0.125 and 0.250 energy continuously increases over two patches and is constant in the area between the two patches. For $L_m/\lambda_b = 0.375$ and 0.50, $\widetilde{E}$ increases over the first patch, but decreases over the second patch in such a way that it gains a maximum in the area between the two patches: that is, energy is trapped in this area. To see the behaviour of the amplitude of each mode, we show in figure 8(*b,c*) the spatial evolution of the amplitudes of transmitted and reflected resonant modes (first five modes, i.e. modes 1, 3, 5, 7 and 9) over the two patches of ripples with $L_m/\lambda_b = 0.50$. Similar to the energy density, amplitudes of all modes consistently increase over the first patch, and in a similar way decrease over the second patch. Interestingly, at the end of the second patch, all the energy is back to the original incident wave energy: an upstream/downstream observer sees absolutely no trace of the two seabed patches on the upstream/downstream wave field.

The behaviour of energy is also a function of the number of ripples in the patch as well as the number of ripples in the neighbouring patch. For a total number of ripples in both patches equal to $n_r = 8$, we show in figure 8(*d–f*) how energy density changes at the beginning of the first patch $\widetilde{E}(0)$, between the two patches $\widetilde{E}(n_{r1}\lambda_b)$ and at the end of the second patch $\widetilde{E}[(n_{r1} + n_{r2} + q)\lambda_b + L_m]$. In all cases, energy at the beginning of the first and at the end of the second patch obtains a global minimum for $L_m/\lambda_b = 0.5$. For the area between the two patches, energy is maximum for $L_m/\lambda_b = 0.5$. The energy density upstream and downstream of the two patch system is only a function of the total number of ripples and not a function of how they are distributed in the two patches.
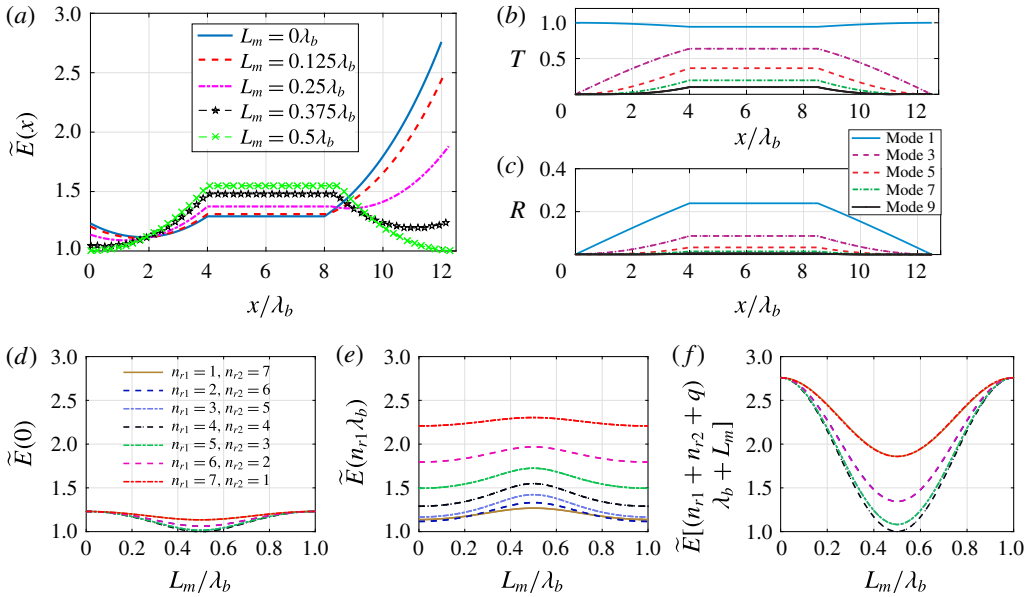
FIGURE 8. (Colour online) (*a*) The spatial evolution of energy density $\widetilde{E}$ in a two patch system with $n_{r1} = n_{r2} = 4$ (cf. figure 1) for different distances between the two patches $L_m/\lambda_b = 0, 0.125, 0.25, 0.375$ and 0.5. The normalized amplitude of seabed corrugations is 0.04. The maximum energy between the two patches is obtained when $L_m/\lambda_b = 0.5$ and the maximum energy at the end of the second patch is obtained for $L_m/\lambda_b = 0$. (*b,c*) Spatial evolution of amplitude of the first five resonant modes (modes 1, 3, 5, 7 and 9) over the two patches of ripples with $L_m/\lambda_b = 0.5$. (*d–f*) Evolution of energy as a function of distance between two patches (*d*) at the beginning of the first patch, (*e*) between two patches and (*f*) at the end of the second patch.

We also consider the effect of the change in the wavenumber of the second patch as shown in figure 9 for two cases where the second patch wavenumber is (i) $k_{b2} = 2.03$ (left column) and (ii) $k_{b2} = 2.1$ (right column). Compared to figure 8, it can be seen that there is still an increase of energy between two patches, while the case where all the waves except the incident mode disappear is not observed.

5. Concluding remarks

We presented here, analytically supported by direct simulation, that the energy distribution of internal waves over a patch of seabed undulations can be strongly dependent upon the distance of the patch to the neighbouring seabed features. Specifically, we considered two neighbouring features: a second patch of seabed undulations and a vertical wall (a perfect reflector). We showed that accumulation of internal waves energy may be an order of magnitude larger or smaller at specific areas of a patch, solely based on where the neighbouring feature is. The wall or the second patch, with specific properties and placement, can also completely cancel the effect of the first patch in such a way that upstream and downstream observers see no trace of the patch in their local wave field. The phenomenon elucidated here may influence, potentially significantly, the distribution of internal waves energy near steep oceanic ridges and continental slopes. In our case studies and simulations, without loss of generality, we considered an incident mode 1 internal wave. Similar results
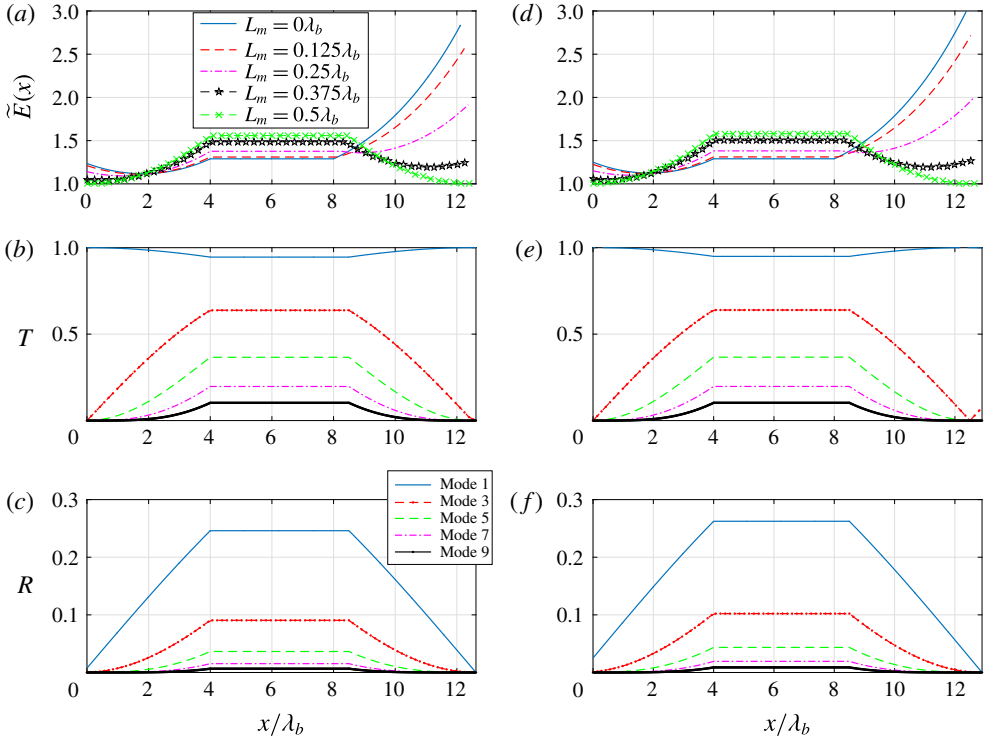
FIGURE 9. (Colour online) (a) The spatial evolution of energy density $\widetilde{E}$ in a two patch system with $n_{r1} = n_{r2} = 4$ and $k_{b1} = 2$ and $k_{b2} = 2.03$ (cf. figure 1) for different distances between the two patches $L_m/\lambda_b = 0$, 0.125, 0.25, 0.375 and 0.5. The normalized amplitude of seabed corrugations is 0.04. (b,c) Spatial evolution of amplitude of the first five resonant modes (modes 1, 3, 5, 7 and 9) over the two patches of ripples with $L_m/\lambda_b = 0.5$. (d) The spatial evolution of energy density $\widetilde{E}$ in a two patch system with $n_{r1} = n_{r2} = 4$ and $k_{b1} = 2$ and $k_{b2} = 2.1$ for different distances between the two patches $L_m/\lambda_b = 0$, 0.125, 0.25, 0.375 and 0.5. (e,f) Spatial evolution of amplitude of the first five resonant modes (modes 1, 3, 5, 7 and 9) over the two patches of ripples with $L_m/\lambda_b = 0.5$.

are obtained for an incident internal wave of any mode if proper conditions between the seabed and the incident internal wave hold.

It is worth noting that density stratification in real oceans is seldom linear and therefore N is not constant and is in fact a function of the depth z (e.g. Simpson 1971; Sigman, Jaccard & Haug 2004). The assumption of a linear density profile, nevertheless, is used extensively either as an approximation to the density profile in the ocean, or to extract the fundamental physics of internal waves (e.g. Thorpe 1966; Klymak, Legg & Pinkel 2010; Lim, Ivey & Jones 2010; Bühler & Holmes-Cerfon 2011; Li & Mei 2014; Guo & Holmes-Cerfon 2016). Although a nonlinear density profile affects the mode shapes of internal waves, the first-order Bragg reflection and hence the resonance condition are unaffected, i.e. for resonance to occur the topography wavenumber will still be twice as large as the wavenumber of the overpassing internal waves. Also, if the number of seabed undulations is large enough, the entire energy will be reflected. In a recent study, Liang, Zareei & Alam (2017) studied the deviation from a linear density profile and it was shown that for

parabolic and exponential profiles of density, the detuning of higher Bragg reflections from perfect resonance is negligible.

While practical aspects of the fundamental study presented here are beyond the scope of the current manuscript, we would like to briefly comment on some potential applications in real oceans. The oceanic internal wave spectrum 'occupies a continuum in scales', including a large number of waves with different frequencies and wavelengths which are clearly results of several mechanisms at play including what was discussed here (cf. Garrett & Munk 1972, 1975). Likewise, the seabed topography is typically irregular but can be decomposed into its Fourier components that in many cases have a few dominant peaks (Cox & Sandstrom 1962). Each Fourier component of the seabed, therefore, can resonate some of the waves in the internal waves spectrum through exact and near resonance mechanisms. Therefore, it may be expected that in real oceans with a broadband wave spectrum and a general irregular topography, multiple resonances occur at the same time leading to a complicated cascade of energy exchanged between modes and even chaos (e.g. Alam, Liu & Yue 2009*b*, §4.4).

Seabed features with periodic or near-periodic structures, as well, are found in many parts of the ocean (see e.g. Nicolas 2013; Simarro *et al.* 2015). For example, the outer shelf of the east China sea (depth of $O(100)$ m) has sand ridges of tens of metres in amplitude spread over hundreds of kilometres. They are believed to have formed during the sea level rise some 10 000 years ago (Chang-shu & Jia-song 1988; Wu *et al.* 2005). Another example is the Sable Island bank off the coast of Nova Scotia that has a system of ridges of $\sim O(10)$ m tall, with a wavelength of $\sim O(2000)$ m located in a water depth that reaches up to 80 m (Boczar-Karakiewicz, Amos & Drapeau 1990). At a larger scale, abyssal hills are ubiquitous, for instance covering some 80 % of the Pacific (abyssal hills are sometimes referred to as the most widespread topological features on the Earth Menard 1964; Buck & Poliakov 1998).

Internal gravity waves have also been observed in a wide range of wavelengths. For instance, in the Baltic and North sea, there have been a number of observations of short-period internal waves with wavelengths of ~ 5000 m with ~ 10 m maximum vertical displacement, and off the coast of Japan, short internal waves have been reported with ~ 2000 m wavelengths and 82 m maximum vertical displacement (see Roberts 1975, and references therein). In both areas, diurnal and semi-diurnal waves have also been observed and reported, but with much larger wavelengths.

Internal waves are well known to be significantly affected by seabed irregularities (e.g. Baines 1998). The influence may be through linear and/or nonlinear mechanisms (e.g. resonance, instabilities, etc.). Internal waves, on the other hand, may be in charge in shaping sand ridges in the shallower waters of continental shelves in areas covered with sand and soft mud (e.g. Boczar-Karakiewicz *et al.* 1990). Internal waves are also known to (usually partially) reflect back from straight and steep slopes, unless in the case of critical reflection in which the reflected beam is along the slope and therefore does not carry energy away from the boundary (Cacchione & Wunsch 1974; Eriksen 1982; Maas *et al.* 1997).

The present study highlights the importance of coupling between these two effects: (i) internal waves scattering by the topography and (ii) the reflection from steep slopes. The trapping and amplification mechanism studied here may lead to spikes in the oceanic internal waves spectrum near continental slopes and steep oceanic ridges (e.g. 3 km tall Kaena Ridge in Hawaii (Klymak, Pinkel & Rainville 2008)) that are next to small mean-seabed irregularities. As discussed above, in real ocean

both internal waves and the seabed contain typically a broad band of wavenumbers. Since the phenomenon studied here is linear, therefore the effect of each Fourier mode of the seabed on corresponding mode(s) of the internal wave spectrum must be superimposed to obtain the overall picture.

Acknowledgements

Appendix A. Details of direct simulation implementation

A.1. *Spatial and temporal discretization*

We use FEM to solve for the streamfunction field in the whole domain. To that end, we first introduce an auxiliary variable ϕ and rewrite the governing equation as:

$$\frac{\partial^2 \phi}{\partial t^2} + N^2 \frac{\partial^2 \psi}{\partial x^2} = 0, \tag{A 1}$$

$$\phi - \Delta \psi = 0. \tag{A 2}$$

In order to solve for the unknown (ϕ, ψ) using FEM, we rewrite the system in its weak form using test function (ϕ^*, ψ^*). The variational formulation (after integration by parts) thus reads

$$\iint_\Omega \left[\frac{\partial^2 \phi}{\partial t^2} \phi^* - N^2 \frac{\partial \psi}{\partial x} \frac{\partial \phi^*}{\partial x} + \phi \psi^* + \boldsymbol{\nabla}\psi : \boldsymbol{\nabla}\psi^* \right] \mathrm{d}\Omega$$
$$+ \int_{\partial\Omega} [N^2(\psi n_x)\phi^* - (\boldsymbol{\nabla}\psi \cdot \boldsymbol{n})\psi^*] \, \mathrm{d}(\partial\Omega) = 0, \tag{A 3}$$

where $\boldsymbol{n}$ is the outward normal vector to $\partial\Omega$ and Ω and $\partial\Omega$ are respectively the bulk and boundaries of the numerical domain. As the next step, this equation is discretized in time using a second-order implicit scheme. With the notation $(\phi(t_n), \psi(t_n)) = (\phi_n, \psi_n)$ and the time step δt, the variational formulation thus becomes

$$\iint_\Omega \left[(\phi_{n+1}\phi^* - 2\phi_n\phi^* + \phi_{n-1}\phi^*)/2\delta t^2 - \frac{N^2}{2} \left(\frac{\partial \psi_{n+1}}{\partial x} + \frac{\partial \psi_{n-1}}{\partial x} \right) \frac{\partial \phi^*}{\partial x} \right] \mathrm{d}\Omega$$
$$+ \iint_\Omega \left[\frac{1}{2}(\phi_{n+1} + \phi_{n-1})\psi^* + \frac{1}{2}\boldsymbol{\nabla}\psi_{n+1} : \boldsymbol{\nabla}\psi^* + \frac{1}{2}\boldsymbol{\nabla}\psi_{n-1} : \boldsymbol{\nabla}\psi^* \right] \mathrm{d}\Omega$$
$$+ \int_{\partial\Omega} \left[\frac{N^2}{2}(\psi_{n+1}n_x + \psi_{n-1}n_x)\phi^* - \frac{1}{2}(\boldsymbol{\nabla}\psi_{n+1} + \boldsymbol{\nabla}\psi_{n-1}) \cdot \boldsymbol{n}\psi^* \right] \mathrm{d}(\partial\Omega) = 0. \tag{A 4}$$

To close the system, we apply the following boundary conditions:

(i) The upper and lower boundaries are the streamlines $\psi_{n+1} = 0$ at all times.
(ii) The inlet is a wavemaker generating a right-travelling incident mode 1 interval wave: $\psi_0(z, t_n) = \hat{\psi}_0 \sin(k_z z) \cos(k_x x_{in} - \omega t_n)$.
(iii) The outlet is a perfectly reflecting wall, i.e. $u = 0$. Therefore, ψ is constant along the wall. Given that the wall intersects the upper and lower boundaries, we have $\psi = 0$ for the reflecting wall.

This equation is then projected on a set of shape functions (which are the same as the test functions) chosen as quadratic P_2 elements over the triangle which constitute the mesh. We apply a mesh refinement in the region close to the ripples and the wall, where the interactions between the internal waves and the domain features are important. The spatial discretization and the time resolution of the resulting discrete equations is done via the open source finite element solver FreeFem++ (Hecht 2012).

Note that the numerical domain is chosen long enough for the establishment of the steady state. A study of the inlet distance to the first ripples reveal that $L = 15\lambda_1$ is sufficient; λ_1 being the wavelength of the incident mode 1 wave. Last, in order to observe Bragg reflection, the seabed corrugation has a wavelength $\lambda_b = \lambda_1/2$. We choose $\delta t = 0.1$ s (note that the scheme is unconditionally stable, but the precision depends on δt) for which convergence is shown to occur and we solve for a time domain $t \in [0, T]$ where $T \sim 2L/C_g$, with C_g the group velocity of mode 1 incident wave. In other words, we stop the simulation approximately when the incoming energy from the wavemaker has been reflected by the wall and returned to the inlet.

A.2. *Computation of the energy distribution*

In order to compute the kinetic and potential energy distribution over the patch and compare with analytical predictions, we first need to obtain the velocity and density fields through the following (discretized) equations: $u_{n+1} = \partial\psi_{n+1}/\partial z$, $w_{n+1} = -\partial\psi_{n+1}/\partial x$, $\rho'_{n+1} = \rho'_{n-1} - (N^2\rho_o/g)((\partial\psi_{n+1}/\partial x) + (\partial\psi_{n-1}/\partial x))\delta t$ where ρ_o is the density at the free surface. At the steady state, $E^k(x)$ and $E^p(x)$ are the kinetic and potential energies of an internal wave integrated in the vertical z-direction. They are computed by averaging the instantaneous energies E^k_{n+1} and E^p_{n+1} over the last p-periods $T_p = p(2\pi/\omega)$ (typically $p = 5$). The integrals are approximated by a trapezoidal rule in time and a three-point Gauss quadrature in z over each triangle edge adjacent to the vertical boundary, i.e.:

$$E^k(x) = \frac{1}{T_p} \sum_{t=0}^{t=T_p} \left\{ \sum_{s=1}^{N_t} \sum_{g=1}^{3} \frac{\rho_o}{2H} \left[\frac{w_{n+1}(z_g)^2 + w_n(z_g)^2}{2} + \frac{u_{n+1}(z_g)^2 + u_n(z_g)^2}{2} \right] \beta_g \right\} \delta t \quad (A\,5)$$

$$E^p(x) = \frac{1}{T_p} \sum_{t=0}^{t=T_p} \left\{ \sum_{s=1}^{N_t} \sum_{g=1}^{3} \frac{g^2}{2H\rho_o N^2} \left[\frac{\rho'_{n+1}(z_g)^2 + \rho'_n(z_g)^2}{2} \right] \beta_g \right\} \delta t, \quad (A\,6)$$

where z_g and β_g are respectively the Gauss quadrature points and their associated weights. Here $N_t = 38$ is the number of triangle edges used to discretize the inlet lateral boundary.

REFERENCES

ALAM, M.-R., LIU, Y. & YUE, D. K. P. 2009*a* Bragg resonance of waves in a two-layer fluid propagating over bottom ripples. Part I. Perturbation analysis. *J. Fluid Mech.* **624**, 191–224.

ALAM, M.-R., LIU, Y. & YUE, D. K. P. 2009*b* Bragg resonance of waves in a two-layer fluid propagating over bottom ripples. Part II. Numerical simulation. *J. Fluid Mech.* **624**, 225–253.

ALAM, M.-R., LIU, Y. & YUE, D. K. P. 2010 Oblique sub-and super-harmonic Bragg resonance of surface waves by bottom ripples. *J. Fluid Mech.* **643**, 437–447.

ANSONG, J. K., ARBIC, B. K., BUIJSMAN, M. C., RICHMAN, J. G., SHRIVER, J. F. & WALLCRAFT, A. J. 2015 Indirect evidence for substantial damping of low-mode internal tides in the open ocean. *J. Geophys. Res.: Oceans* **120**, 6057–6071.

BAINES, P. G. 1971*a* The reflexion of internal/inertial waves from bumpy surfaces. *J. Fluid Mech.* **46**, 273–291.

BAINES, P. G. 1971*b* The reflexion of internal/inertial waves from bumpy surfaces. Part 2. Split reflexion and diffraction. *J. Fluid Mech.* **49**, 113–131.

BAINES, P. G. 1998 *Topographic Effects in Stratified Flows*. Cambridge University Press.

BALMFORTH, N. J. & PEACOCK, T. 2009 Tidal conversion by supercritical topography. *J. Phys. Oceanogr.* **39**, 1965–1974.

BELL, T. H. 1975*a* Lee waves in stratified flows with simple harmonic time dependence. *J. Fluid Mech.* **67**, 705–722.

BELL, T. H. 1975*b* Topographically generated internal waves in the open ocean. *J. Geophys. Res.* **80**, 320–327.

BOCZAR-KARAKIEWICZ, B., AMOS, C. L. & DRAPEAU, G. 1990 The origin and stability of sand ridges on Sable Island Bank, Scotian Shelf. *Cont. Shelf Res.* **10**, 683–704.

BRAGG, W. H. & BRAGG, W. L. 1913 The reflection of X-rays by crystals. *Proc. R. Soc. Lond.* A **88**, 428–438.

BUCK, W. R. & POLIAKOV, A. N. B. 1998 Abyssal hills formed by stretching oceanic lithosphere. *Nature* **392**, 272–275.

BÜHLER, O. & HOLMES-CERFON, M. 2011 Decay of an internal tide due to random topography in the ocean. *J. Fluid Mech.* **678**, 271–293.

CACCHIONE, D. & WUNSCH, C. 1974 Experimental study of internal waves over a slope. *J. Fluid Mech.* **66**, 223–239.

CHANG-SHU, Y. & JIA-SONG, S. 1988 Tidal sand ridges on the East China Sea shelf. In *Tide-Influenced Sedimentary Environments and Facies*, pp. 23–38. Springer.

COUSTON, L.-A., GUO, Q., CHAMANZAR, M. & ALAM, M.-R. 2015 Fabry–Pérot resonance of water waves. *Phys. Rev.* E **92**, 043015.

COUSTON, L.-A., JALALI, M. A. & ALAM, M.-R. 2017 Shore protection by oblique seabed bars. *J. Fluid Mech.* **815**, 481–510.

COUSTON, L.-A., LIANG, Y. & ALAM, M.-R. 2016 Oblique internal-wave chain resonance over seabed corrugations, arXiv:1604.07308.

COX, C. & SANDSTROM, H. 1962 Coupling of internal and surface waves in water of variable depth. *J. Oceanogr. Soc. Japan* **18**, 499–513.

ERIKSEN, C. C. 1982 Observations of internal wave reflection off sloping bottoms. *J. Geophys. Res.: Oceans* **87**, 525–538.

FABRY, C. & PÉROT, A. 1897 Sur les franges des lames minces argentees et leur application a la mesure de petites epaisseurs d'air. *Ann. Chim. Phys.* **12**, 459–501.

FERMI, E. & MARSHALL, L. 1947 Interference phenomena of slow neutrons. *Phys. Rev.* **71**, 666.

FRINGER, O. B., GERRITSEN, M. & STREET, R. L. 2006 An unstructured-grid, finite-volume, nonhydrostatic, parallel coastal ocean simulator. *Ocean Model.* **14**, 139–173.

FRINGER, O. B. & ZHANG, Z. 2008 High-resolution simulations of nonlinear internal gravity waves in the South China Sea. In *DoD HPCMP Users Group Conference, 2008. DOD HPCMP UGC*, pp. 43–46. IEEE.

GARABATO, A. C. N., POLZIN, K. L., KING, B. A., HEYWOOD, K. J. & VISBECK, M. 2004 Widespread intense turbulent mixing in the Southern Ocean. *Science* **303**, 210–213.

GARGETT, A. E. & HOLLOWAY, G. 1984 Dissipation and diffusion by internal wave breaking. *J. Mar. Res.* **42**, 15–27.

GARRETT, C. & MUNK, W. 1972 Space-time scales of internal waves. *Geophys. Astrophys. Fluid Dyn.* **3**, 225–264.

GARRETT, C. & MUNK, W. 1975 Space-time scales of internal waves: a progress report. *J. Geophys. Res.* **80**, 291–297.

GUO, Y. & HOLMES-CERFON, M. 2016 Internal wave attractors over random, small-amplitude topography. *J. Fluid Mech.* **787**, 148–174.

HECHT, F. 2012 New development in FreeFem++. *J. Numer. Math.* **20**, 251–265.

KANG, D. & FRINGER, O. 2012 Energetics of barotropic and baroclinic tides in the Monterey Bay area. *J. Phys. Oceanogr.* **42**, 272–290.

KLYMAK, J. M., LEGG, S. M. & PINKEL, R. 2010 High-mode stationary waves in stratified flow over large obstacles. *J. Fluid Mech.* **644**, 321–336.

KLYMAK, J. M., PINKEL, R. & RAINVILLE, L. 2008 Direct breaking of the internal tide near topography: Kaena ridge, Hawaii. *J. Phys. Oceanogr.* **38**, 380–399.

KRANENBURG, C., PIETRZAK, J. D. & ABRAHAM, G. 1991 Trapped internal waves over undular topography. *J. Fluid Mech.* **226**, 205–217.

KRYUCHKYAN, G. & HATSAGORTSYAN, K. 2011 Bragg scattering of light in vacuum structured by strong periodic fields. *Phys. Rev. Lett.* **107**, 1–4.

KUNDU, P. K., COHEN, I. M. & DOWLING, D. R. 2012 *Fluid Mechanics*. Academic.

LABEUR, R. J. & PIETRZAK, J. D. 2004 Computation of non-hydrostatic internal waves over undular topography. In *Shallow Flows*, pp. 187–194.

LAMB, K. G. 2014 Internal wave breaking and dissipation mechanisms on the continental slope/shelf. *Annu. Rev. Fluid Mech.* **46**, 231–254.

LEDWELL, J. R., MONTGOMERY, E. T., POLZIN, K. L., ST. LAURENT, L. C., SCHMITT, R. W. & TOOLE, J. M. 2000 Evidence for enhanced mixing over rough topography in the abyssal ocean. *Nature* **403**, 179–182.

LI, Y. & MEI, C. C. 2014 Scattering of internal tides by irregular bathymetry of large extent. *J. Fluid Mech.* **747**, 481–505.

LIANG, Y., ZAREEI, A. & ALAM, M.-R. 2017 Inherently unstable internal gravity waves due to resonant harmonic generation. *J. Fluid Mech.* **811**, 400–420.

LIM, K., IVEY, G. N. & JONES, N. L. 2010 Experiments on the generation of internal waves over continental shelf topography. *J. Fluid Mech.* **663**, 385–400.

MAAS, L. R. M., BENIELLI, D., SOMMERIA, J. & LAM, F.-P. A. 1997 Observation of an internal wave attractor in a confined, stably stratified fluid. *Nature* **388**, 557–561.

MATHUR, M., CARTER, G. S. & PEACOCK, T. 2014 Topographic scattering of the low-mode internal tide in the deep ocean. *J. Geophys. Res.: Oceans* **119**, 2165–2182.

MATHUR, M. & PEACOCK, T. 2010 Internal wave interferometry. *Phys. Rev. Lett.* **104**, 118501.

MEI, C. C. 1985 Resonant reflection of surface water waves by periodic sandbars. *J. Fluid Mech.* **152**, 315–335.

MENARD, H. W. 1964 *Marine Geology of the Pacific*. McGraw-Hill.

MIED, R. P. & DUGAN, J. P. 1976 Internal wave reflexion from a sinusoidally corrugated surface. *J. Fluid Mech.* **76**, 259–272.

MÜLLER, P. & LIU, X. 2000a Scattering of internal waves at finite topography in two dimensions. Part I: theory and case studies. *J. Phys. Oceanogr.* **30**, 532–549.

MÜLLER, P. & LIU, X. 2000b Scattering of internal waves at finite topography in two dimensions. Part II: spectral calculations and boundary mixing. *J. Phys. Oceanogr.* **30**, 550–563.

NICOLAS, A. 2013 *The Mid-oceanic Ridges: Mountains Below Sea Level*. Springer Science & Business Media.

PIETRZAK, J. & LABEUR, R. J. 2004 Trapped internal waves over undular topography in a partially mixed estuary. *Ocean Dyn.* **54**, 315–323.

PIETRZAK, J. D., KRANENBURG, C., ABRAHAM, G., KRANENBORG, B. & VAN DER WEKKEN, A. 1991 Internal wave activity in Rotterdam waterway. *J. Hyd. Engng* **117**, 738–757.

ROBERTS, J. 1975 *Internal Gravity Waves in the Ocean*. Marcel Dekker.

SIGMAN, D. M., JACCARD, S. L. & HAUG, G. H. 2004 Polar ocean stratification in a cold climate. *Nature* **428**, 59–63.

SIMARRO, G., GUILLÉN, J., PUIG, P., RIBÓ, M., IACONO, C. L., PALANQUES, A., MUÑOZ, A., DURÁN, R. & ACOSTA, J. 2015 Sediment dynamics over sand ridges on a tideless mid-outer continental shelf. *Mar. Geol.* **361**, 25–40.

SIMPSON, J. H. 1971 Density stratification and microstructure in the western Irish sea. *Deep Sea Res. Oceanogr. Abst.* **18**, 309–319.

STASTNA, M. 2011 Resonant generation of internal waves by short length scale topography. *Phys. Fluids* **23**, 1–10.

THORPE, S. A. 1966 On wave interactions in a stratified fluid. *J. Fluid Mech.* **24**, 737–751.

WANG, B., FRINGER, O. B., GIDDINGS, S. N. & FONG, D. A. 2009 High-resolution simulations of a macrotidal estuary using SUNTANS. *Ocean Model.* **28**, 167–192.

WU, Z., JIN, X., LI, J., ZHENG, Y. & WANG, X. 2005 Linear sand ridges on the outer shelf of the East China Sea. *Chin. Sci. Bulletin* **50**, 2517–2528.

YU, J. & MEI, C. C. 2000 Do longshore bars shelter the shore? *J. Fluid Mech.* **404**, 251–268.